Fatigue behavior of additive manufactured 316L stainless steel under axial versus rotating-bending loading: Synergistic effects of stress gradient, surface roughness, and volumetric defects

Rakish Shrestha [a,b], Jutima Simsiriwong [b,c], Nima Shamsaei [a,b,*]

[a] *Department of Mechanical Engineering, Auburn University, Auburn, AL 36849, USA*
[b] *National Center for Additive Manufacturing Excellence (NCAME), Auburn University, Auburn, AL 36849, USA*
[c] *School of Engineering, University of North Florida, Jacksonville, FL 32224, USA*

ARTICLE INFO

ABSTRACT

In this study, the stress gradient effects on the fatigue behavior of 316L stainless steel (SS) specimens fabricated using two different laser beam-powder bed fusion (LB-PBF) processes were investigated, with an emphasis on the surface roughness and volumetric defects. The fatigue behavior of LB-PBF 316L SS largely depended on the applied stress amplitude. Under higher stress amplitudes, rotating-bending specimens generally exhibited better fatigue resistance as compared to the axial specimens subjected to the same nominal stresses. At lower stress amplitudes, the surface roughness and/or volumetric defects became more significant life-limiting factors for LB-PBF 316L SS.

1. Introduction

Fatigue testing methods utilizing axial (i.e., tension–compression) and rotating-bending (R-B) loadings are commonly used for conventionally or AM produced materials. Comparing to the R-B test method, the axial fatigue testing, which is typically conducted with a servohydraulic system, offers more flexibility to control and monitor the loading signals (i.e., strain, force, displacement with different minimum to maximum load ratios) [1]. On the other hand, the electro-mechanical R-B fatigue testing is usually limited to the fully-reversed, force-controlled, constant amplitude loading, which is typically performed at higher test frequencies as compared to axial fatigue testing. Since the R-B fatigue test system is considerably lower in cost, less expensive to operate, and can be used to generate data at a faster rate than the axial fatigue test system, it is a particularly attractive to obtain relatively quick fatigue experimental data, which has also been used to generate fatigue data for different metallic AM materials [2,3].

Generally, for wrought metallic materials, a smooth and unnotched specimen under R-B loading is expected to have a better fatigue resistance than the one subjected to axial loading with the same nominal stress [4,5]. The lower fatigue resistance in the axial specimen is primarily due to the difference in the stress distribution across the cross-sectional area of the specimen's gage. As illustrated in Fig. 1, the normal stress due to axial loading is uniformly distributed throughout the gage cross-sectional area. On the other hand, the stress gradient exists in the R-B specimen. The normal stress due to the bending moment decreases linearly from its maximum value at the surface to zero at the specimen's neutral axis [1,6], as displayed in Fig. 1.

Urashima et al., [7] evaluated the low cycle fatigue (LCF) behavior of three different types of traditionally-fabricated steel alloys with and without the presence of a surface notch. The specimens were subjected to R-B and axial fatigue tests. Significantly higher fatigue resistance was reported in all notched and un-notched steel specimens under R-B loading. Interestingly, under the same nominal stress, a higher strain amplitude was measured at the surface of the specimens under axial loading as compared to those under R-B loading. This observation was contributed to the lower fatigue resistance in axial specimens. Furthermore, a good correlation of the fatigue data from R-B and axial loadings was obtained by considering the plastic strain amplitude as the damage parameter [7].

The stress gradient effects on fatigue behavior in the LCF regime of two different types of aluminum alloys were quantitatively studied by Abel [8]. It was reported that the stress at the crack tip in the specimens

---

Nomenclature

K_f	Fatigue stress concentration factor
R_a	Arithmetic mean roughness value
R_z	Maximum valley depth below the average line
R_σ	Ratio of minimum to maximum stress
σ_a	Stress amplitude
$2N_f$	Reversals to failure

Table 1

Major process parameters utilized for fabrication of 316L SS specimens using two LB-PBF AM machines.

		Laser power (W)	Scanning speed (mm/s)	Hatching space (µm)	Layer thickness (µm)
Machine A	Filling	200	1000	110	50
	Contour	110	1250	N/A	50
Machine B	Filling	195	1083	90	20
	Contour	110	800	N/A	20

subjected to R-B loading was impacted by the crack length. For example, for the crack with the length equal to 6.13% of the specimen's radius, the stress at the crack tip was reported to be 1.84% lower than the applied stress. On the other hand, the stress at the crack tip in the specimens subjected to axial cyclic loading continuously increased, which could result in a higher crack growth rate, and ultimately, a lower fatigue resistance under axial loading relative to those under R-B loading [8].

In addition, in the axial fatigue testing, the entire specimen gage is subjected to uniform axial stress that could lead to inadequate dissipation of hysteresis energy, resulting in the increase in temperature of the specimen and decrease in fatigue resistance [1]. Since the specimen under axial loading has a larger material volume that experiences the maximum stress as compared to the specimen subjected to R-B loading, there is also a greater probability of crack initiation in the axial specimen due to the higher number of statistically distributed material anomalies [1]. Nonetheless, a knock-down factor of 0.75 and 0.9 has been established to correct for the fatigue limit under axial loading based on the fatigue limit obtained from small wrought metallic specimens (i.e., specimens with gage diameter less than 10 mm) subjected to R-B cyclic loading [1].

Despite many research efforts focusing on investigating the mechanical behavior of AM parts under cyclic loading, to the best of the authors' knowledge, the differences between their fatigue behavior under R-B and axial loadings have not been yet reported. AM parts are known to have high surface roughness due to the layer-wise manufacturing fabrication as well as the presence of partially-melted powder particles along the part's surface [9–11]. They are also susceptible to various volumetric defects such as lack of fusion (LoF) defects and entrapped gas pores [11–15]. Since the stress is not uniformly distributed across the cross-section of the specimen subjected to R-B loading, the aforementioned surface roughness and the distribution of volumetric defects in AM parts could play an important role in their fatigue performance. Furthermore, the surface roughness and volumetric defects in AM parts are also affected by many factors particularly the employed process parameters, which are typically varied from one manufacturing machine to another [16].
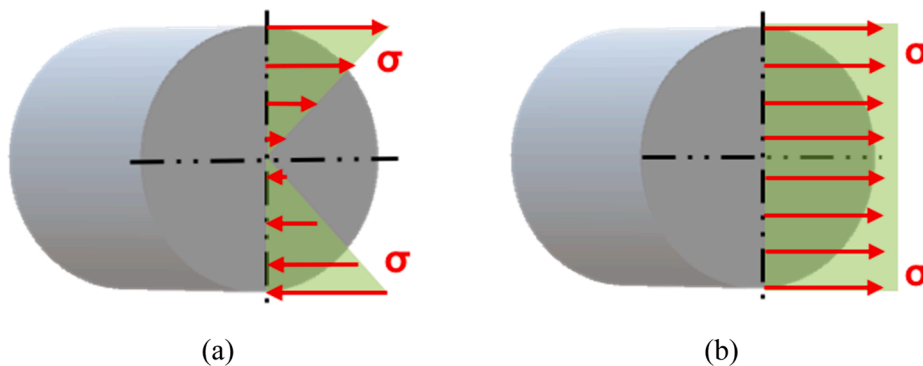
In this study, the effects of stress gradient, surface roughness, and volumetric defects, as affected by the AM platform used for part fabrication, on the fatigue behavior of 316L stainless steel (SS) were synergistically investigated. Two laser beam-powder bed fusion (LB-PBF) AM platforms are employed in this study to fabricate specimens with different levels of surface roughness and volumetric defects. The selected material, 316L SS, is widely used in marine applications, nuclear power plants, and internal fixation biomedical implants. This is due to its biocompatibility, and excellent corrosion and wear resistance [17–20]. Following the introduction in this study, the material, fabrication, and experimental procedures are described, and the experimental results are presented. Stress gradient, surface roughness, and porosity effects on the fatigue behavior of LB-PBF 316L SS are then discussed with accompanied fractography analysis. Finally, the major conclusions derived from the experimental results are presented.

2. Material, fabrication, and experimental procedures

2.1. Material and specimens fabrication

Two different LB-PBF AM platforms, which will be referred to as Machine A and Machine B throughout this work, were used to fabricate fatigue specimens. The specimens were made utilizing Argon atomized 316L SS powder, supplied by LPW Inc., with particle size distribution ranging from 15 to 45 µm. All specimens were fabricated in a vertical direction (i.e., perpendicular to the build plate) in an argon environment with the recommended filling and contour process parameters for 316L SS as tabulated in Table 1. It should be noted that these recommended major process parameters for both machines were mostly similar except for the layer thickness (50 µm for Machine A and 20 µm for Machine B).

LB-PBF 316L SS cylindrical rods and near net-shaped specimens were fabricated using the geometries presented in Fig. 2. The cylindrical rods were further machined using a computer numerical control lathe into two types of specimens. These are (1) specimens with reduced gage section (i.e., hourglass specimens) for R-B fatigue test (see Fig. 2(a) based on ISO 1143 [21], and (2) specimens with uniform gage section for the axial fatigue test (see Fig. 2(b) based on ASTM Standard E-466 [22]. It should be noted that the fatigue stress concentration factor for R-
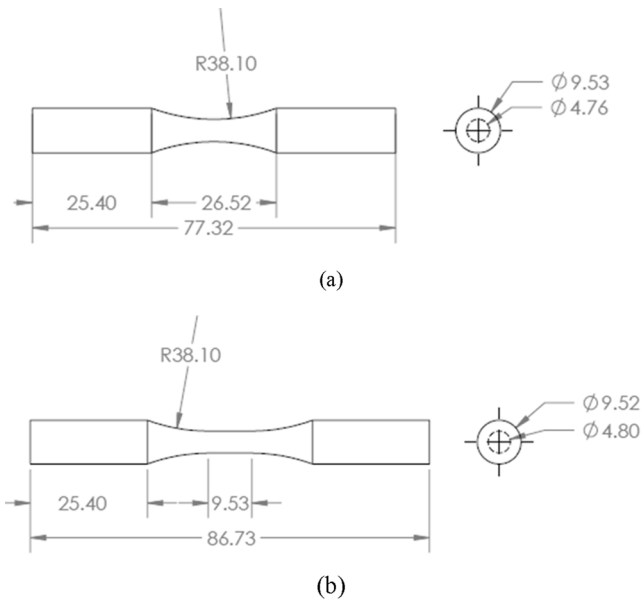

(a)   (b)

Fig. 1. Schematic showing the normal stress distribution on the circular cross-section of the specimen gage due to (a) R-B and (b) axial loadings, assuming the linear elastic deformation.

(a)

(b)

Fig. 2. The geometry and dimensions of specimens used for (a) rotating-bending test based on ISO Standard 1143 [21] and (b) axial test based on ASTM Standard E-466 [22]. All the dimensions are in mm.

B specimens due to the reduced gage section is very small (i.e., $K_f = 1.009$), which is less than 1%. All specimens with as-built (AB) surface condition (i.e., near net-shaped specimens) and machined specimens were further subjected to solution annealing at 1038 °C for one hour in a vacuum environment, then air-cooled to room temperature. This heat treatment procedure was chosen to replicate that of the wrought 316L SS

used in this study for comparison purposes. Following the heat treatment, machined specimens were further polished using sandpapers ranging from 800, 1500, and 2000 grits to remove any machining marks, and these specimens will be referred to as machined and polished (M/P) specimen throughout the paper.

2.2. Testing setup

All fatigue tests were conducted under the fully-reversed ($R_\sigma = -1$) loading condition with stress amplitudes ranging from 250 to 350 MPa. R-B fatigue tests were performed using a System Integrators RBF-200 machine at a constant frequency of 50 Hz in the cantilevered-type setup. Axial fatigue tests were conducted on an MTS servo-hydraulic test frame with a 100 kN load cell with test frequencies varying between 4.6 and 6.5 Hz. The frequencies in the axial fatigue tests were varied to maintain a similar average cyclic stress rate, while all tests under R-B loading were conducted at 50 Hz. Although the test frequencies are significantly different, these are the typical applied frequencies for each type of fatigue test method. Therefore, any possible influence of the applied frequency on the fatigue resistance of LB-PBF 316L SS is considered to be part of the test setup.

All experiments in this study were performed at room temperature and relative humidity. Furthermore, fractography analysis to determine the factors responsible for crack initiation and failure mechanisms, and the surface roughness measurements were conducted using a Keyence VHX 6000 digital microscope. Surface roughness parameters were determined using the average values obtained from line roughness measurements at five different locations. All fracture surfaces were sonicated prior to conducting the fractography analysis to remove any dust particles.

Table 2
Fatigue test results of LB-PBF 316L SS subjected to rotating bending (R-B) and axial loadings along with the defect characteristics responsible for crack initiation. The specimens were fabricated using Machine A.

Loading Type	Surface Condition	σ_a(MPa)	Specimen ID	2N$_f$ (reversals)	Surface Condition	σ_a(MPa)	Specimen ID	2N$_f$ (reversals)	Defect size (µm)	Type	Location
R-B	AB	250	MA_RB AS8	748,200	M/P	250	MA_RB MS9	1,448,200	59/25/20	Pore and LoF	Surface
			MA_RB AS9	1,704,800			MA_RB MS7	1,547,800	123	LoF	Surface
		300	MA_RB AS7	407,600		300	MA_RB MS6	621,200	133/90	LoF	Surface
							MA_RB MS5	815,600	137/72	LoF	Surface
		325	MA_RB AS1	250,800		325	MA_RB MS4	479,400	132/75/24	Pore and LoF	Surface
			MA_RB AS2	193,600			MA_RB MS3	1,027,400	48/44	LoF	Sub-surface
		350	MA_RB AS5	139,000		350	MA_RB MS2	263,200	295	LoF	Surface
			MA_RB AS6	207,400			MA_RB MS1	477,400	181	LoF	Surface
Axial	AB	250	MA_Ax AS8	537,030	M/P	250	MA_Ax MS1	3,649,582	87	LoF	Surface
			MA_Ax AS7	785,320			MA_Ax MS2	> 4,000,000	N/A	N/A	N/A
		300	MA_Ax AS9	141,474		300	MA_Ax MS3	1,061,322	64	LoF	Surface
			MA_Ax AS6	166,220			MA_Ax MS4	2,737,092	49	LoF	Surface
		325	MA_Ax AS1	37,818		325	MA_Ax MS5	156,804	207	LoF	Surface
			MA_Ax AS3	44,390			MA_Ax MS6	314,896	74	LoF	Surface
		350	MA_Ax AS4	6,856		350	MA_Ax MS7	84,400	61	LoF	Surface
			MA_Ax AS5	10,650			MA_Ax MS8	85,588	57	LoF	Surface

Table 3

Fatigue test results of LB-PBF 316L SS subjected to rotating bending (R-B) and axial loadings along with the defect characteristics responsible for crack initiation. The specimens were fabricated using Machine B.

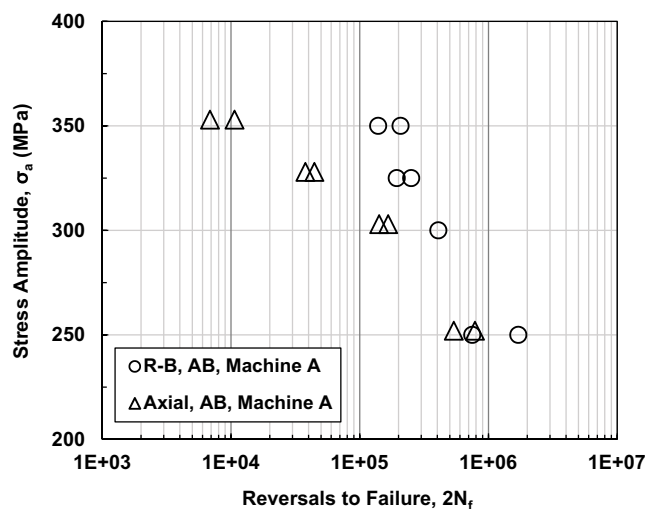| Loading Type	Surface Condition	σ_a(MPa)	Specimen ID	$2N_f$ (reversals)	Surface Condition	σ_a(MPa)	Specimen ID	$2N_f$ (reversals)	Defect size (μm)	Type	Location
R-B	AB	250	MB_RB AS5	331,400	M/P						
			MB_RB AS7	413,800							
		300	MB_RB AS4	242,200							
			MB_RB AS3	259,200							
		325	MB_RB AS10	98,000		325	MB_RB MS6	> 4,000,000	N/A	N/A	N/A
			MB_RB AS8	109,200			MB_RB MS7	> 4,000,000	N/A	N/A	N/A
		350	MB_RB AS2	74,200		350	MB_RB MS4	1,678,000	26	Pore	Sub-surface
			MB_RB AS1	89,600			MB_RB MS5	> 4,000,000	N/A	N/A	N/A
Axial	AB	250	MB_Ax AS2	834,196	M/P						
			MB_Ax AS1	934,848							
		300	MB_Ax AS4	221,326		300	MB_Ax MS3	> 4,000,000	N/A	N/A	N/A
			MB_Ax AS3	274,214			MB_Ax MS4	> 4,000,000	N/A	N/A	N/A
		325	MB_Ax AS5	66,340		325	MB_Ax MS6	1,288,006	N/A	N/A	N/A
			MB_Ax AS6	76,138			MB_Ax MS5	1,432,854	22	Pore	Surface
		350	MB_Ax AS8	7,968		350	MB_Ax MS7	65,962	N/A	N/A	N/A
			MB_Ax AS7	11,648			MB_Ax MS8	81,642	14	Pore	Surface

Fig. 3. Stress amplitudes versus fatigue lives obtained under rotating-bending (R-B) and axial loadings for LB-PBF 316L SS specimens, fabricated using Machine A, in as-built (AB) surface condition.

3. Experimental results and discussions

To investigate the synergistic effects of stress gradient, surface roughness, and volumetric defects on the fatigue behavior of LB-PBF 316L SS, specimens in AB and M/P surface conditions were subjected to R-B and axial loading. Furthermore, as the surface roughness and volumetric defects are affected by the AM platform used for part fabrication, R-B and axial fatigue testing were also conducted on specimens fabricated using two different LB-PBF platforms (i.e., Machine A and Machine B). The fatigue data, including the applied stress amplitude, σ_a, and reversals to failure, $2N_f$, obtained for all specimens (i.e., specimens in AB and M/P surface conditions subjected to R-B and axial loading) fabricated using Machine A and Machine B are tabulated in Tables 2 and 3, respectively. Additional information on the defect characteristics including their type, size, and location for the specimens in M/P surface condition are also included in these Tables. The size of the defects was calculated based on the Murakami approach using the square root of the area of the circle surrounding the defect on the plane of maximum normal stress [23]. The defect characteristics in AB specimens are not presented in these tables since all fatigue cracks were observed to initiate from the surface.

3.1. Effects of stress gradient

Stress amplitudes versus fatigue lives for LB-PBF 316L SS specimens in AB surface condition fabricated using Machine A are shown in Fig. 3. In general, AB specimens exhibited better fatigue lives under R-B loading as compared to those subjected to axial loading. This observation is prominent at higher stress amplitudes (i.e., 325 and 350 MPa), where the larger portion of life is spent in the fatigue crack growth stage. All fatigue cracks in R-B and axial specimens in Fig. 3 were found to initiate from the micro-notches at the surface, which is expected for AM parts with no post-processing machining [24–27]. Once cracks initiate from the surface, cracks in specimens under R-B loading do not grow as fast due to a decrease in stress (i.e., stress gradient) as cracks grow away from the surface, resulting in better fatigue performance at higher stress amplitudes relative to the axial specimens. It is also important to mention that, due to the high ductility inherent to 316L SS, the specimens may experience large plastic deformation at higher stress amplitudes. Therefore, the stress may be mostly uniform in the vicinity of the

surface; however, as cracks propagate away from the surface, the nominal stress is expected to be gradually reduced.

Fracture surfaces obtained for the AB R-B specimen (with $2N_f = 250,800$ reversals) and the AB axial specimen (with $2N_f = 44,390$ reversals) subjected to stress amplitude of 325 MPa are shown in Figs. 4(a) and 4(b), respectively. In general, the fracture surfaces observed in both types of specimens in AB surface condition closely resemble the fracture surfaces reported for notched wrought specimens [1]. In both loading cases, fatigue cracks were observed to initiate from the micro-notches located at the surface of the specimen. Furthermore, from the micro-scopy images of the fracture surfaces, the surface quality of R-B and axial specimens were also visibly similar, which was further supported by the surface roughness analysis. The arithmetic mean roughness values, R_a, and value of maximum valley depth below the average line, R_z, for both R-B specimens (i.e., hourglass specimens) and axial specimens (i.e., specimens with uniform gage section) fabricated using Machine A were determined to be $R_a \approx 10$ μm and $R_z \approx 44$ μm.

A distinct variation in the fracture surface was evident by a higher number of crack initiation sites in the R-B specimen as compared to the axial specimen. This can be explained by the fact that, under R-B loading, the stress decreases as the crack propagates from the surface. The delay in fatigue crack propagation would allow the initiation of other cracks on the surface [28]. In addition, the area of crack propagation is observed to be larger in the R-B specimen, resulting in a smaller final fracture region as compared to the axial specimen. From the fractography analysis, the region of final fracture in the R-B (Fig. 4 (a)) and axial (Fig. 4(b)) specimens are found to be approximately 0.82 and 3.2 mm^2, respectively. This can be also explained by the fact that the stress at the tip of the crack in R-B specimen is smaller than the one in axial specimen when final fracture occurs.

From the higher magnification optical images shown in Fig. 4, all fatigue cracks were observed to initiate from the surface (indicated by red dotted arrows in the higher magnification images) of the specimens even in the presence of entrapped gas pores (indicated by red circles). These pores were primarily located close to the surface with an average diameter of approximately 40 μm. Hence, this observation may indicate that the surface roughness can be more detrimental to the fatigue behavior of LB-PBF 316L SS specimens as compared to the presence of near-surface entrapped gas pores, regardless of the testing method. It is also important to note that the higher detrimental effect of surface roughness compared to the volumetric defects can diminish in the presence of larger LoF defects [29]. Studies have shown similar fatigue lives for AB and M/P specimens, where M/P specimens fail due to large LoF defects [11].

As the microstructure, as well as the process-induced defects and their distribution in AM parts can vary depending on the employed
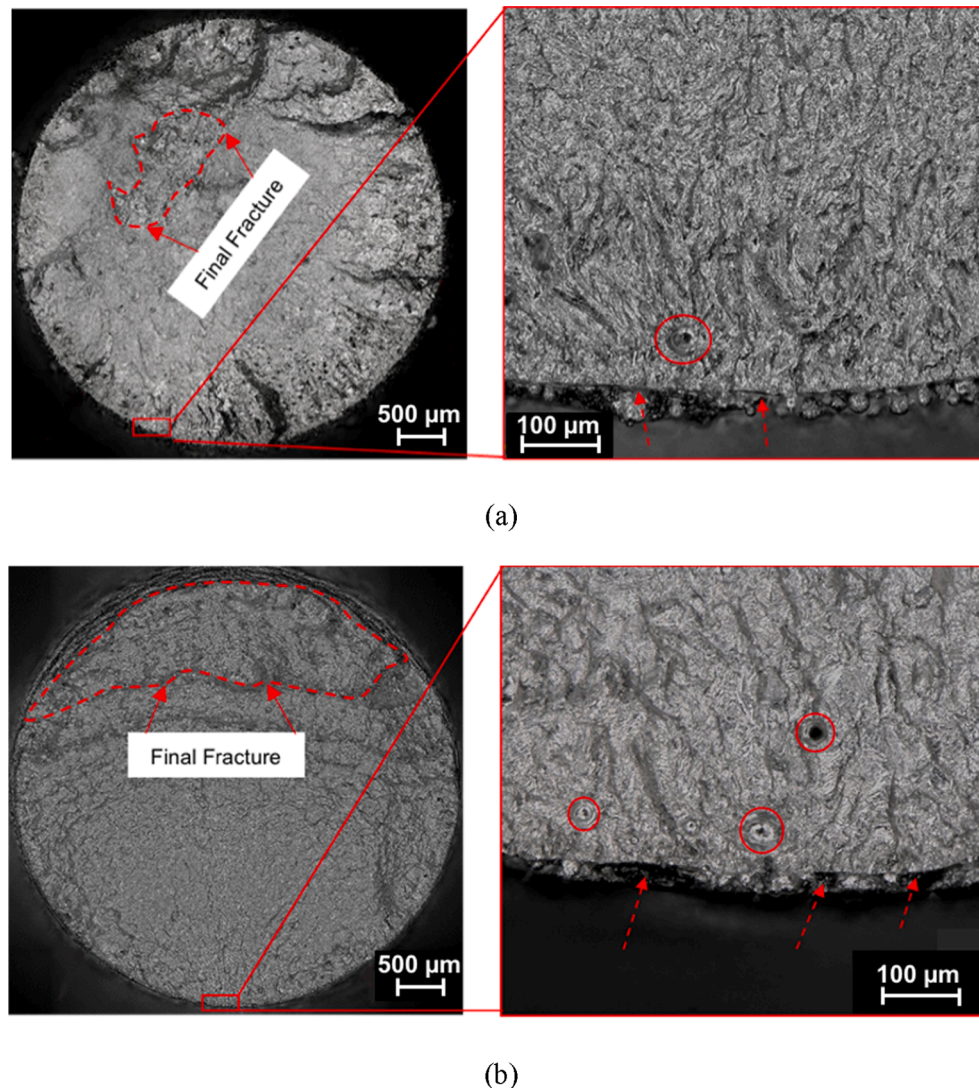

(a)

(b)

Fig. 4. Fracture surfaces of specimens in as-built (AB) surface condition subjected to (a) R-B loading with $2N_f = 250,800$ reversals and (b) axial loading with $2N_f = 44,390$ reversals. Both specimens were fabricated using Machine A, and tested at 325 MPa stress amplitude.

process parameters and manufacturing machine, fatigue tests were also conducted on AB LB-PBF 316L SS specimens fabricated using Machine B. The test results are presented in Fig. 5. A similar observation can be obtained from this figure where R-B specimens subjected to higher stress amplitudes (i.e., 325 and 350 MPa) generally exhibited better fatigue

Fig. 5. Stress amplitudes versus fatigue lives obtained under rotating-bending (R-B) and axial loadings for LB-PBF 316L SS specimens, fabricated using Machine B, in as-built (AB) surface condition.

resistance as compared to the axial specimens. The difference in fatigue lives reduces as the applied stress amplitude decreases. At the lower stress amplitude of 250 MPa, the axial specimens exhibited longer fatigue lives, at least by a factor of two, as compared to the R-B specimens.

Fracture surfaces of LB-PBF 316L SS specimens in AB surface condition fabricated via Machine B subjected to R-B and axial loadings at the stress amplitude of 250 MPa are shown in Figs. 6(a) and 6(b), respectively. Similar to the AB specimens fabricated using Machine A, all fatigue cracks in Fig. 6 were initiated from the micro-notches at the surface. In addition, the surface roughness of the R-B specimen in this image was visibly higher than that of the axial specimen. Upon further analysis, the arithmetic mean roughness values, R_a, were determined to be 14 and 10 µm and maximum valley depth below the average line, R_z, to be 52 and 44 µm, respectively, for R-B and axial specimens fabricated using Machine B.

The influences of stress gradient on the fatigue life of AB specimens subjected to lower stress amplitudes (i.e., 250 and 300 MPa) may not be quite as significant as compared to the specimens subjected to higher stress amplitudes. Since a larger portion of fatigue life at lower stress amplitudes is governed by the crack initiation stage, the lower crack growth rate due to the stress gradient in R-B specimens may not be as effective in enhancing their fatigue resistance. As a result, at lower stress amplitude, the influence of surface roughness on the fatigue behavior of AB specimens could be greater as compared to the stress gradient effect. For specimens in Fig. 6, thus, the lower surface roughness may have resulted in longer fatigue life in the axial specimen ($2N_f = 834,196$ reversals) when compared to the R-B specimen ($2N_f = 413,800$ reversals). In addition, it should be noted that R-B specimens are hourglass shaped,
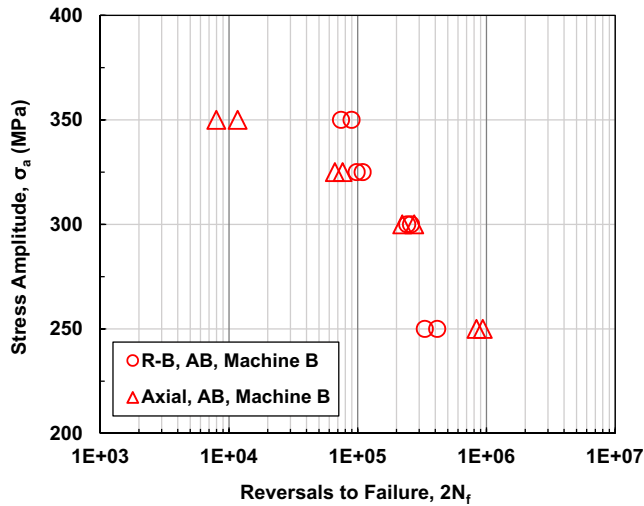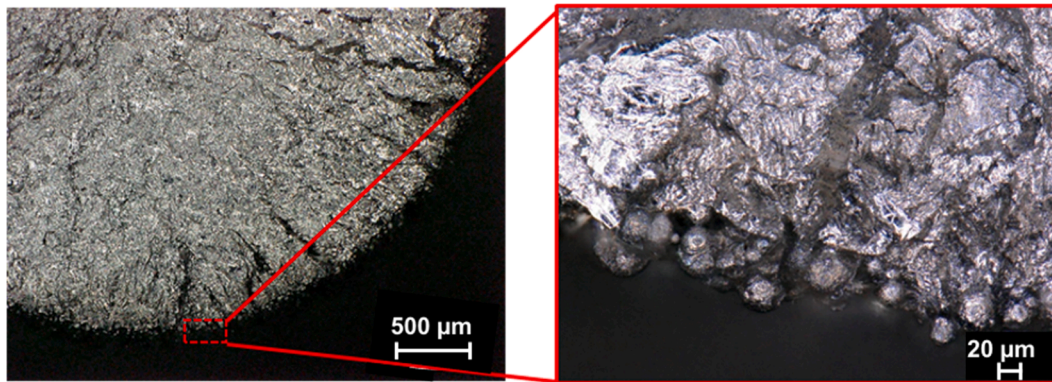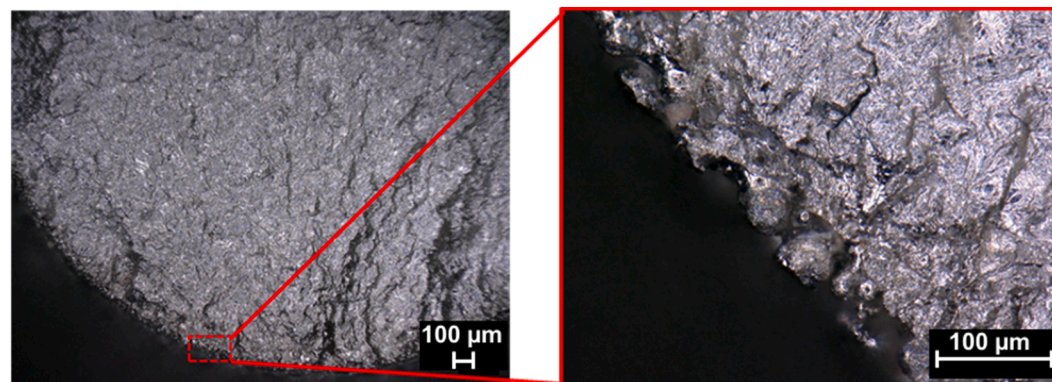

(a)

(b)

Fig. 6. Fracture surfaces showing the differences in the surface roughness for (a) the R-B specimen with $R_a = 14$ µm and $2N_f = 413,800$ reversals, and (b) an axial specimen with $R_a = 10$ µm and $2N_f = 834,196$ reversals. Both specimens were fabricated using Machine B, and tested at 250 MPa stress amplitude.

while axial specimens have a uniform gage section. The differences in the specimens' geometry could also result in the variation in thermal history [10,30,31], which can ultimately affect the surface roughness of the specimen's gage section.

In the absence of surface roughness, volumetric defects and their distributions are considered to be a major life-limiting factor in AM parts

Fig. 7. Stress amplitude versus fatigue lives obtained under rotating-bending (R-B) and axial loadings for LB-PBF 316L SS specimens, fabricated using Machine A, in M/P surface condition.

[32–36]. Hence, the influences of stress gradient on the fatigue resistance of AM parts are also expected to be affected by these volumetric defects. As a result, R-B and axial tests were also conducted on the specimens with M/P surface condition. The fatigue data of M/P specimens fabricated using Machine A are shown in Fig. 7. Similar to those observed in AB specimens (see Figs. 3 and 5), the effect of the stress gradient appears to vary depending on the applied stress amplitude. Higher fatigue resistance was exhibited by specimens subjected to R-B loading at higher stress amplitudes, but not when specimens were subjected to lower stress amplitudes. This again can be attributed to the greater influence of stress gradient and lower sensitivity to the presence of defects on the fatigue behavior at higher stress amplitudes as compared to lower stress amplitudes.

Fracture surfaces that reveal factors responsible for crack initiation and failure for M/P R-B and axial specimens fabricated using Machine A are presented in Fig. 8. Both specimens were subjected to a nominal stress amplitude of 300 MPa. As seen in Fig. 8(a) and 8(b), the crack initiated from multiple LoF defects in the R-B specimen ($2N_f = 815,600$ reversals), while the fatigue crack initiated from a single LoF defect in the case of specimen subjected to axial loading ($2N_f = 2,737,092$ reversals). This higher number of crack initiating defects, which was also observed in other R-B specimens, may have been responsible for shorter fatigue lives at lower stress amplitudes, which is more sensitive to the presence of volumetric defects, and where a less portion of fatigue life is spent in the crack growth stage.

Fracture surfaces of specimens subjected to R-B and axial loadings at a higher stress amplitude of 350 MPa are shown in Figs. 9(a) and 9(b), respectively. The LoF defect that caused the crack initiation in the R-B
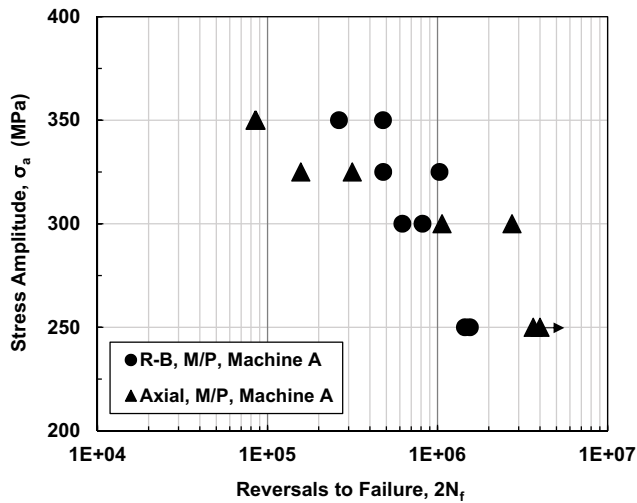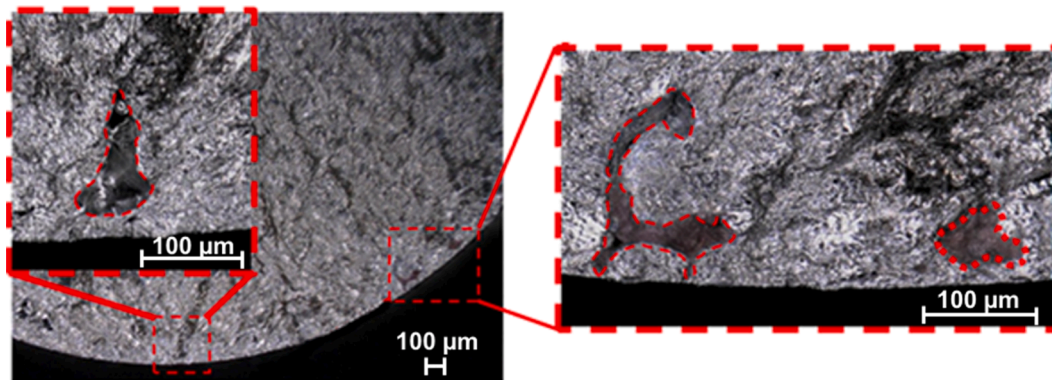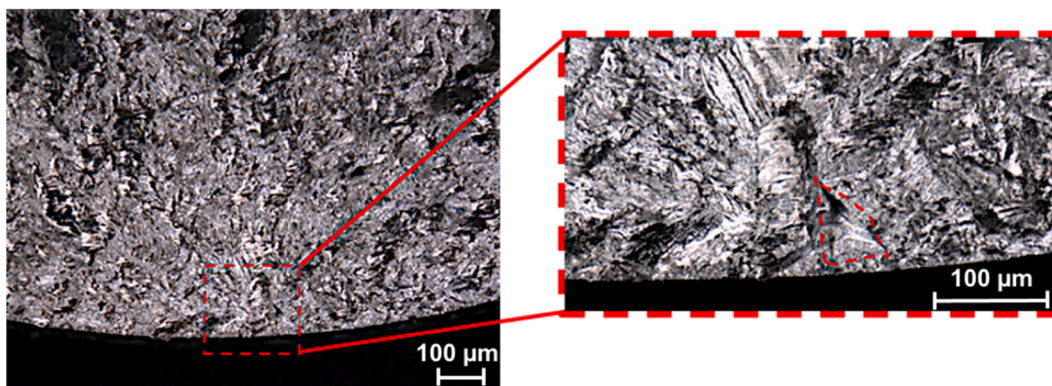

(a)

(b)

Fig. 8. Fracture surfaces showing lack of fusion defects responsible for initiation of crack in specimens subjected to (a) R-B loading with $2N_f = 815,600$ reversals and (b) axial loading with $2N_f = 2,737,092$ reversals. Both specimens were tested at stress amplitude of 300 MPa and fabricated using Machine A.
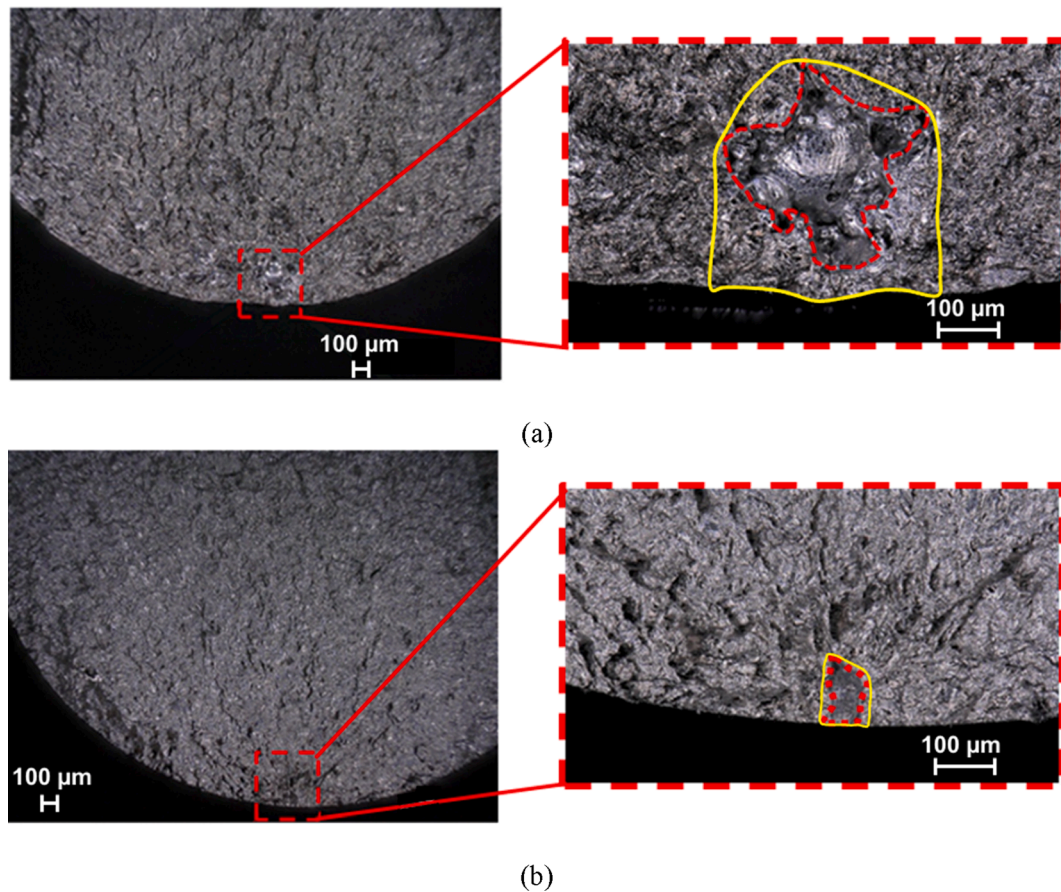
(a)

(b)

Fig. 9. Fracture surfaces showing LoF defects responsible for initiation of crack in specimens with M/P surface condition subjected to (a) R-B loading with $2N_f = 263{,}200$ reversals and (b) axial loading with $2N_f = 84{,}400$ reversals. Both specimens were tested at stress amplitude of 350 MPa and fabricated using Machine A. Red dotted line represents the actual defect size, while yellow solid line is the defect size determined using Murakami's approach. (For interpretation of the references to colour in this figure legend, the reader is referred to the web version of this article.)

specimen was visibly larger as compared to the one in the axial specimen. However, even in the presence of a larger crack initiating defect, the specimen subjected to R-B loading exhibited longer fatigue life as compared to the specimen under axial loading (263,200 reversals versus 84,400 reversals). This observation may also support the fact that at high stresses, where the crack growth stage dominates a larger portion of fatigue life, the effect of stress gradient may be more significant than the effect of defect size.

The next set of fatigue data are shown in Fig. 10(a) for M/P specimens that were fabricated using Machine B. As seen, the specimens exhibited better fatigue resistance under R-B loading as compared to axial loading at different stress levels. It also needs to be mentioned that the specimens fabricated using Machine B reached four million reversals (i.e., the life defined as runout in this study) at 350 and 300 MPa under R-B and axial loadings, respectively. A fracture surface for specimen fabricated using Machine B and subjected to stress amplitude of 325 MPa under axial cyclic loading is shown in Fig. 10(b). A smaller entrapped gas pore, rather than LoF defects, was found to be responsible for the crack initiation in this specimen. Similar observation with the crack initiating from smaller entrapped gas pores were also evident in other specimens fabricated using Machine B.

To investigate the effect of stress gradient in absence of volumetric and surface defects inherent to AM parts, R-B and axial fatigue tests were also conducted on wrought 316L SS, and the results are presented in Fig. 11(a). Wrought specimens were also subjected to an identical annealing process, and similar stress amplitudes that were used for LB-PBF 316L SS specimens. Although it seems that the R-B specimens outperformed the axial specimens at higher stress amplitudes of 425 and

450 MPa, the axial specimens failed due to excessive deformation at the gage section, as illustrated in Fig. 11(b). Accordingly, a good understanding of the stress gradient on the wrought 316L SS as compared to those on LB-PBF 316L SS could not be fully obtained in this study due to a higher amount of plastic deformation in wrought 316L SS specimens at the specified stress amplitudes.

3.2. Effects of surface roughness

The comparisons of the R-B and axial fatigue behavior between LB-PBF 316L SS specimens with AB and M/P surface conditions and fabricated using Machine A are displayed in Fig. 12. As expected, an increase in fatigue resistance of the specimens was observed after post-fabrication machining, irrespective of the type of loading. Although the beneficial effect of machining was evident in most of the test conditions, the differences in fatigue life data between specimens with AB and M/P conditions were seen to be much lower for the specimens subjected to R-B loading (i.e., within a factor of two as shown in Fig. 12(a)), as compared to those under axial loading (i.e., within a factor of seven as shown in Fig. 12(b)).

The lower sensitivity of the fatigue performance to the surface finish condition for the R-B specimens could be explained by two observations. First, fatigue cracks in these specimens were observed to initiate from large LoF defects close to the surface (see Figs. 8 and 9), which may have a similar effect as micro-notches on the AB specimens' surface. Secondly, the role of crack initiation is not as significant under R-B loading as compared to axial loading due to the stress gradient effects. Hence, the beneficial influence of post-fabrication machining was more evident for
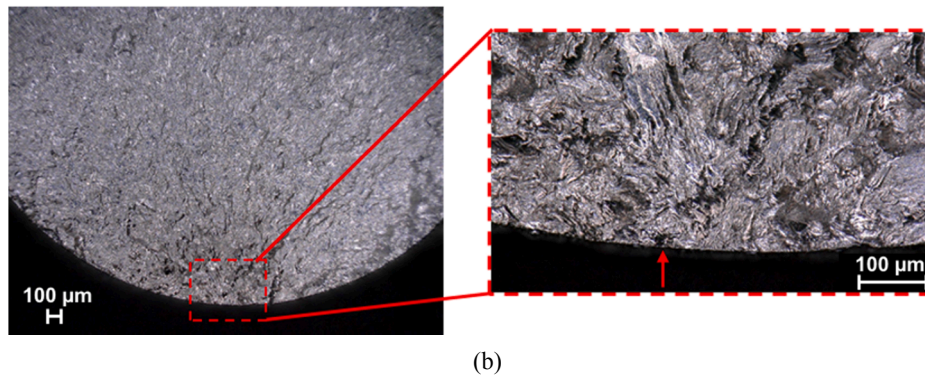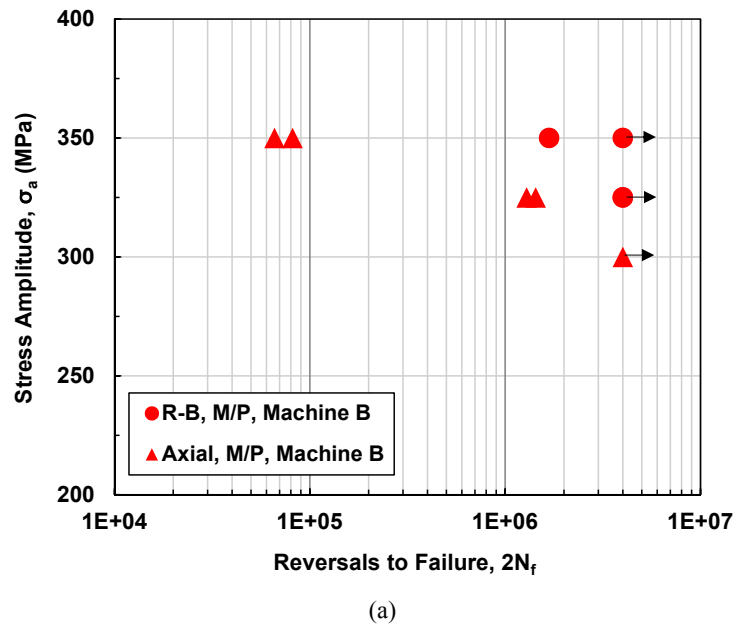
(a)

(b)

Fig. 10. (a) Stress amplitudes versus fatigue lives obtained under rotating-bending (R-B) and axial loadings for LB-PBF 316L SS specimens in M/P surface condition. (b) The fracture surface of a specimen in M/P surface condition subjected to stress amplitude of 325 MPa with $2N_f = 1,432,854$ reversals. All specimens were fabricated using Machine B.

specimens under axial fatigue loading, as displayed in Fig. 12(b).

The effects of surface roughness on LB-PBF 316 SS specimens fabricated using Machine B are shown in Fig. 13. As seen for both loading types, the fatigue resistance of the specimens in M/P surface conditions was observed to be significantly better (up to an order of magnitude) relative to the specimens in AB surface condition. As previously discussed, most fatigue cracks in the M/P specimens fabricated using Machine B initiated from a single entrapped gas pore (see Fig. 10(b)), rather than multiple LoF defects as observed in M/P specimens fabricated using Machine A. Therefore, for those fabricated using Machine B, the absence of LoF defects has caused much better fatigue resistance for M/P specimens, while the micro-notches on the surface of the AB specimens significantly knock-down their fatigue performance.

3.3. Effects of layer thickness

Fatigue-life data obtained at different stress amplitudes for specimens fabricated using Machines A and B in AB surface condition are presented in Fig. 14. Interestingly, under R-B loading, higher fatigue lives were obtained for specimens from Machine A as compared to specimens from Machine B, while under axial loading, not much variations in fatigue lives were observed among specimens fabricated using different LB-PBF platforms.

As mentioned earlier, the R-B tests were conducted using hourglass

specimens, while the axial tests were conducted using specimens with a uniform gage section. This variation in the part geometry was also seen to affect the resulting surface roughness values as the average surface roughness and the maximum valley depth below the average line were higher for hourglass specimens ($R_a = 14$ μm and $R_z = 52$ μm) fabricated using Machine B as compared to the hourglass specimens fabricated using Machine A ($R_a = 10$ μm and $R_z = 46$ μm). The higher surface roughness of hourglass specimens fabricated with Machine B most likely has resulted in their lower fatigue resistance as compared to the ones fabricated using Machine A. On the other hand, in the case of axial specimens with uniform gage section, the surface roughness values for specimens fabricated using Machines A and B are very similar ($R_a \approx 10$ μm and $R_z \approx 44$ μm), resulting in their comparable fatigue lives, as seen in Fig. 14(b).

Interestingly, higher surface roughness was observed for specimens fabricated using Machine B (layer thickness = 20 μm) as compared to those fabricated using Machine A (layer thickness = 50 μm). Such observation is somewhat counter-intuitive as higher surface roughness is typically associated with larger layer thickness. This could be due to the combined effects of the filling process parameters (i.e., layer thickness) and contouring parameters that result in the differences in surface roughness. While a portion of surface roughness comes from layer wise manufacturing, the rest come from partially melted powder particles on the surface, which is highly influenced by the contour parameters.
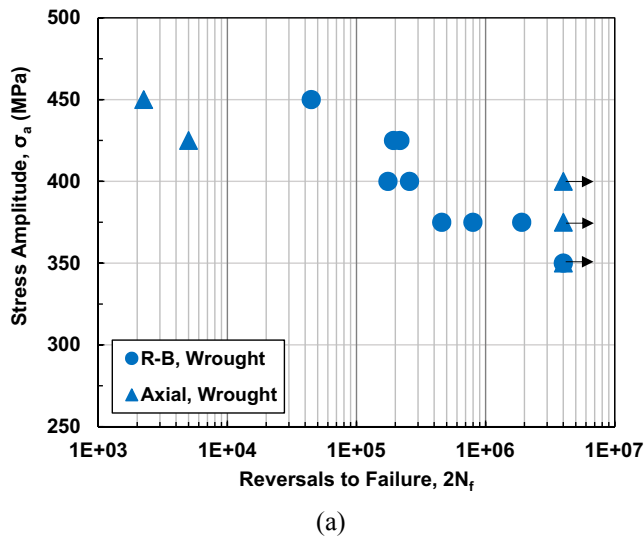
(a)

(b)

Fig. 11. (a) Stress amplitudes versus fatigue lives obtained under rotating-bending (R-B) and axial loadings for wrought 316L SS specimens, and (b) a wrought 316L SS specimen, which was subjected to stress amplitude of 425 MPa and had a fatigue live, $2N_f = 5,780$ reversals. This specimen failed due to excessive deformation at the gage section.

(a)

(b)

Fig. 12. Stress amplitudes versus reversals to failure obtained for LB-PBF 316L SS specimens in as-built (AB) and M/P surface conditions. These specimens were fabricated using Machine A and subjected to (a) rotating-bending (R-B) and (b) axial loadings.

For specimens with M/P surface finish, the fatigue resistance exhibited by specimens fabricated using Machine B was generally superior to that of specimens fabricated using Machine A, irrespective of the loading type, as seen in Fig. 15. The exception of this observation is at the stress amplitude of 350 MPa under axial cyclic loading, where the failures occurred in around 70,000 to 90,000 reversals for specimens from both manufacturing machines. As seen on the fracture surfaces in Figs. 8, 9, and 10, cracks appeared to initiate from larger LoF defects in M/P specimens fabricated using Machine A, whereas those in M/P specimens fabricated using Machine B initiated from a single, smaller entrapped gas pore. This variation in the type, number and size of volumetric defects may be attributed to the difference in the layer thickness used in the two LB-PBF AM platforms.

Since the employed major process parameters, including laser power, scanning speed, and hatch spacing, for Machines A and B are comparable (see Table 1), the morphology of the melt pools (i.e., melt pool depth and overlap depth between the consecutive melt pools) for all LB-PBF 316 SS specimens is also expected to be somewhat similar [37]. However, due to a significant difference in the layer thickness between Machine A (50 μm) and Machine B (20 μm), the ratios of melt pool depth and melt pool overlap depth to layer thickness are anticipated to be
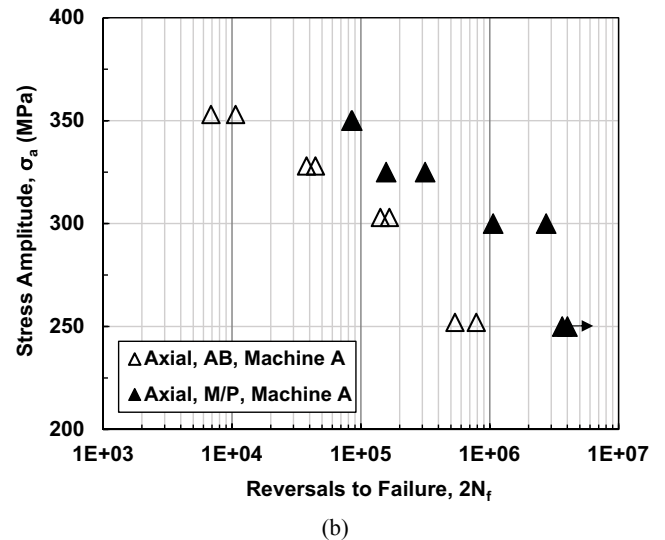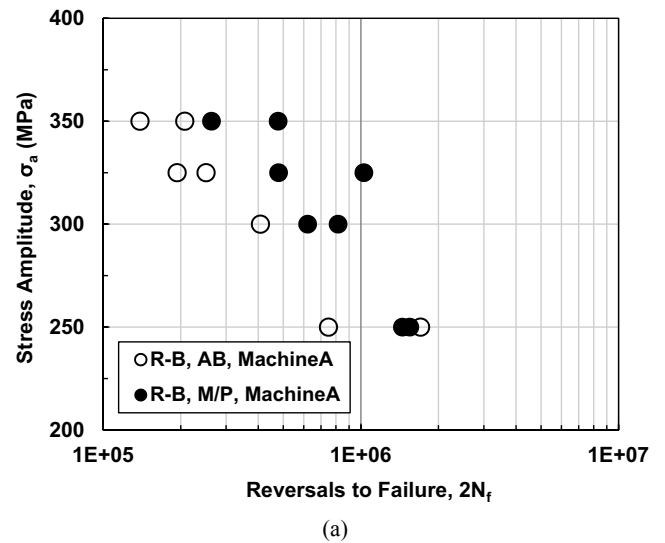
much higher in specimens fabricated using Machine B as compared to Machine A specimens.

Higher ratios of the melt pool depth (or melt pool overlap depth) to the layer thickness suggest that the melt pool can penetrate through multiple layers, resulting in sufficient metallurgical bonding. On the other hand, the lower ratios of the melt pool depth (or overlap depth) to layer thickness can lead to regions with insufficient fusion, and the formation of LoF defects [30,37–40]. Hence, LoF defects were primarily observed on the fracture surfaces of Machine A specimens, whereas they were not observed on the fracture surfaces of Machined B specimens, as illustrated in Tables 2 and 3. It should be noted that when the layer thicknesses are different, considering a much higher thermal conductivity of solidified material versus powder, the size and morphology of the melt pools are expected to be slightly different, even by using similar process parameters. Regardless, when the layer thickness is much higher, there is more possibility of weak metallurgical bonding, leading to the formation of LoF defects.
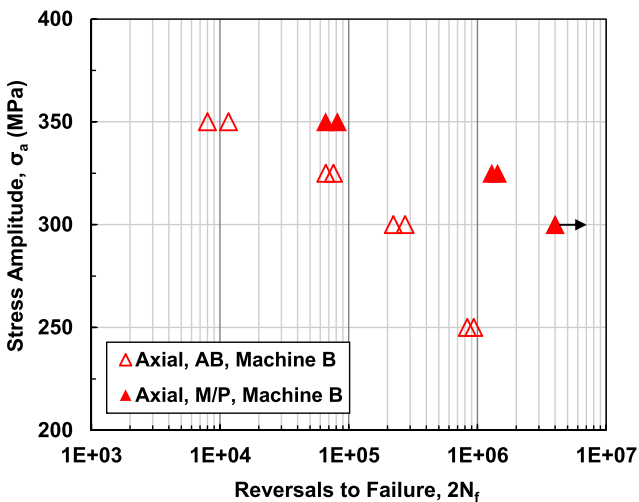
As a result, the differences in fatigue behavior between the specimens fabricated using Machines A and B could arise from the higher detrimental effect of LoF defects in specimens from Machine A, especially at lower stress amplitudes where crack initiating defects play a
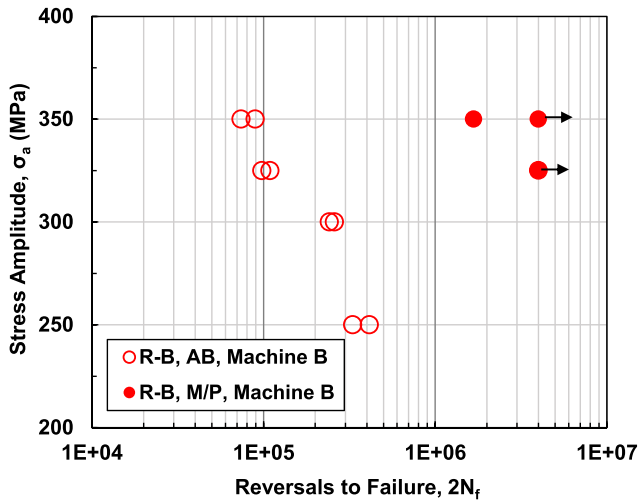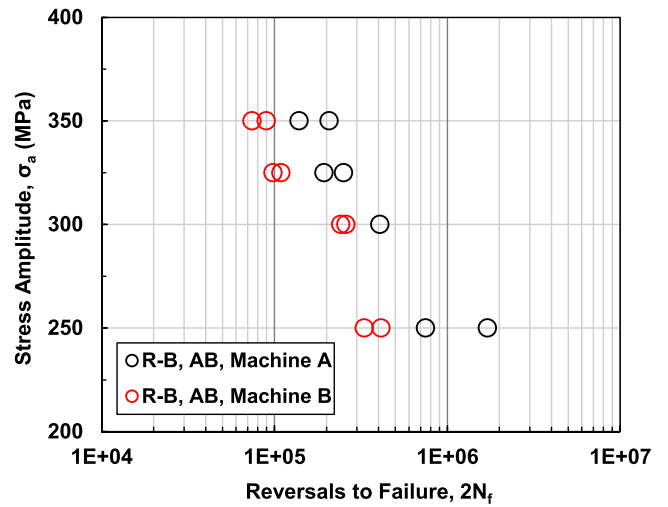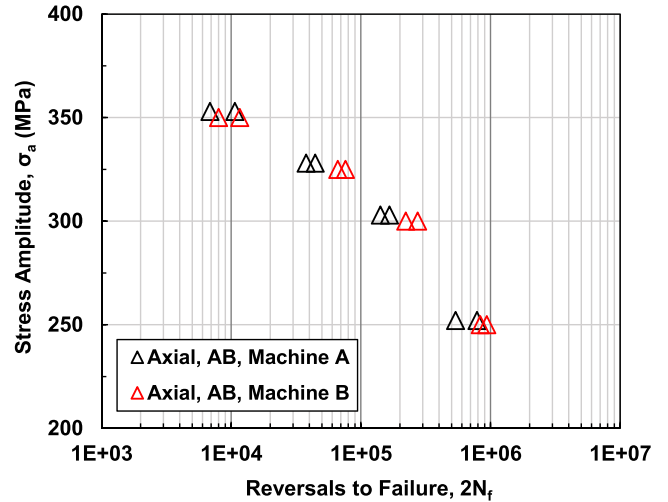
Fig. 13. Stress amplitudes versus reversals to failure obtained for LB-PBF 316L SS specimens in as-built (AB) and M/P surface conditions. These specimens were fabricated using Machine B and subjected to (a) rotating-bending (R-B) and (b) axial loadings.

Fig. 14. Stress amplitudes versus reversals to failure obtained for LB-PBF 316L SS specimens in as-built (AB) surface condition from Machine A and Machine B subjected to (a) rotating-bending (R-B) and (b) axial loadings.

critical role. Conversely, the similarity in fatigue lives at higher stresses with larger plastic deformation may be due to the lower sensitivity of the fatigue resistance to the crack initiating defects. It is also important to note that, in the case of R-B loading, better fatigue resistance was exhibited by the specimens fabricated using Machine B at all stress levels including tests conducted at higher stress amplitudes.

Since the R-B fatigue tests were conducted on specimens with a reduced gage section, the maximum applied stress is experienced within a small volume in the gage section of the specimens. As Machine A specimens contain higher volumetric defects as compared to the specimens fabricated using Machine B, there is a higher probability of detrimental defects existing at the small gage section of Machine A specimens resulting in them exhibiting a lower fatigue resistance in all stress levels relative to Machine B specimens.

4. Conclusions

In the current study, the effects of stress gradient on the fatigue behavior of LB-PBF 316L SS specimens fabricated using two different LB-PBF AM platforms were investigated under the R-B and axial cyclic loading. Fatigue tests were conducted on specimens with AB and M/P

surface conditions to investigate the synergistic effects of stress gradient, surface roughness, and volumetric defects. Based on the experimental results and observations, the following conclusions can be made:

1. Regardless of surface condition, LB-PBF platform, or testing type, fatigue cracks always initiated at or very close to the surface.
2. Irrespective to the surface conditions, the extent of the stress gradient effects on the fatigue behavior of LB-PBF 316L SS specimens appeared to be heavily influenced by the applied stress amplitude. Specimens consistently exhibited better fatigue performance under R-B testing at higher stresses, which was attributed to the more dominating effect of fatigue crack growth stage on the overall fatigue life (i.e., lower fatigue lives).
3. Specimens under R-B loading had a lower crack growth rate due to the stress gradient effect, resulting in them exhibiting longer fatigue lives at higher stresses as compared to specimens under axial loading.
4. Comparing the fatigue behavior of R-B and axial specimens at lower applied stress amplitudes (i.e., 250 and 300 MPa), specimens with higher surface roughness (for AB surface condition), or larger volumetric defects (for M/P surface condition) exhibited lower fatigue performance.
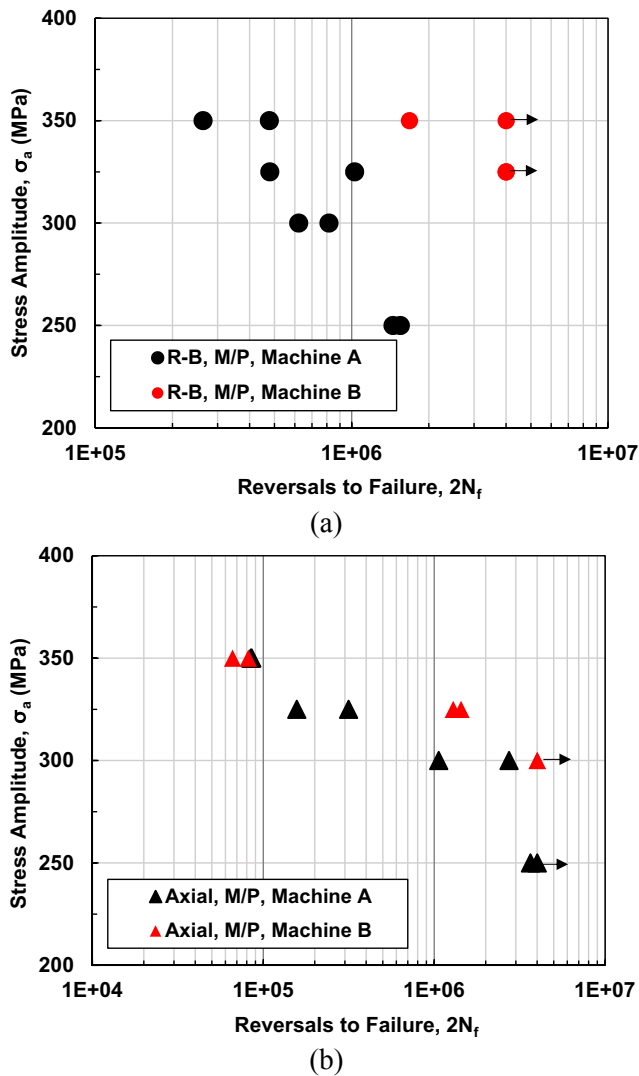
(a)

(b)

Fig. 15. Stress amplitudes versus reversals to failure obtained for LB-PBF 316L SS specimens in M/P surface condition from Machine A and Machine B subjected to (a) rotating-bending (R-B) and (b) axial loadings.

5. For specimens with M/P surface condition, fatigue cracks in both R-B and axial specimens fabricated using Machine A were observed to initiate from LoF defects, while those fabricated using Machine B initiated from smaller entrapped gas pores. As a result, LB-PBF 316L SS specimens from Machine B exhibited superior fatigue resistance, irrespective of the loading type, when compared to those fabricated using Machine A.

6. The differences in the volumetric defects in specimens fabricated using Machines A and B can be associated with the variation in the manufacturer's recommended process parameters, particularly the layer thickness (i.e., 50 μm for Machine A versus 20 μm for Machine B). The larger layer thickness in Machine A results in a lower ratio of melt pool depth to layer thickness, which can cause weak metallurgical bonding between layers, and consequently, LoF defects.

It should be noted that, although the sampling size in this study is limited, the conclusions on the overall fatigue behavior were made base on the general trend. Due to a variation in surface defects (i.e., surface roughness) observed, multiple test replicates for each stress amplitude are recommended to better capture the fatigue behavior of LB-PBF 316L. In addition, since the stress gradient effects on fatigue behavior of LB-PBF 316L SS were observed to be dependent on the fatigue regime, as

well as the surface roughness and volumetric defects that are inherent to the AM processes, the universal correlations between the R-B and axial fatigue limits for wrought metallic materials may not be applicable for AM materials. Therefore, comprehensive experimental data for AM materials may be warranted to obtain the appropriate fatigue correlations between the two types of fatigue testing.

Declaration of Competing Interest

The authors declare that they have no known competing financial interests or personal relationships that could have appeared to influence the work reported in this paper.

Acknowledgments

References

[1] Stephens RI, Fatemi A, Stephens RR, Fuchs HO. Metal fatigue in engineering. John Wiley & Sons; 2000.

[2] Masuo H, Tanaka Y, Morokoshi S, Yagura H, Uchida T, Yamamoto Y, et al. Influence of defects, surface roughness and HIP on the fatigue strength of Ti-6Al-4V manufactured by additive manufacturing. Int J Fatigue 2018;117:163–79.

[3] Uzan NE, Shneck R, Yeheskel O, Frage N. Fatigue of AlSi10Mg specimens fabricated by additive manufacturing selective laser melting AM-SLM. Mater Sci Eng, A 2017;704:229–37.

[4] Eshin A. A method for correlating different types of fatigue curve. Int J Fatigue 1980;2:153–8.

[5] Heywood RB. Designing against fatigue. Chapman and Hall; 1962.

[6] Manson SS. Fatigue: A complex subject—Some simple approximations. Exp Mech 1965;5:193–226.

[7] Urashima C, Nishida S, Ebara R, Yamada Y, Yamamura K. Comparison between rotating bending and push-pull fatigue strength in low cycle region. Low Cycle Fatigue and Elasto-Plastic Behaviour of Materials 1987:538–43.

[8] Abel A. Comparison of low cycle axial, rotating and bending fatigue of aluminium alloys. Low Cycle Fatigue and Elasto-Plastic Behaviour of Materials 1987:610–5.

[9] Lee S, Pegues JW, Shamsaei N. Fatigue behavior and modeling for additive manufactured 304L stainless steel: The effect of surface roughness. Int J Fatigue 2020;141.

[10] Yadollahi A, Shamsaei N. Additive manufacturing of fatigue resistance materials: Challenges and opportunities. Int J Fatigue 2017;98:14–31.

[11] Shrestha R, Simsiriwong J, Shamsaei N. Fatigue behavior of additive manufactured 316L stainless steel: Effects of layer orientation and surface roughness. Addit Manuf 2019;28:23–38.

[12] Daniewicz S, Shamsaei N. An introduction to the fatigue and fracture behavior of additive manufactured parts. Int J Fatigue 2017;2:167.

[13] Yang KV, Rometsch P, Jarvis T, Rao J, Cao S, Davies C, et al. Porosity formation mechanisms and fatigue response in Al-Si-Mg alloys made by selective laser melting. Mater Sci Eng, A 2018;712:166–74.

[14] Pegues JW, Shao S, Shamsaei N, Sanaei N, Fatemi A, Warner DH, et al. Fatigue of additive manufactured Ti-6Al-4V, Part I: The effects of powder feedstock, manufacturing, and post-process conditions on the resulting microstructure and defects. Int J Fatigue 2020;132:105358.

[15] Clymer DR, Cagan J, Beuth J. Power–velocity process design charts for powder bed additive manufacturing. J Mech Des 2017;139:100907.

[16] Gao W, Zang Y, Ramanujan D, Ramani K, Chen Y, Williams CB, et al. The status, challenges, and future of additive manufacturing in engineering. Comput Aided Des 2015;69.

[17] Harun WSW, Kamariah MSIN, Muhamad N, Ghani SAC, Ahmad F, Mohamed Z. A review of powder additive manufacturing processes for metallic biomaterials. Powder Technol 2018;327:128–51.

[18] Dewidar MM, Khalil KA, Lim J. Processing and mechanical properties of porous 316L stainless steel for biomedical applications. Transactions of Nonferrous Metals Society of China 2007;17:468–73.

[19] Bajaj P, Hariharan A, Kini A, Kürnsteiner P, Raabe D, Jägle EA. Steels in additive manufacturing: A review of their microstructure and properties. Mater Sci Eng, A 2020;772.

[20] Singh S, Ramakrishna S, Singh R. Material issues in additive manufacturing: A review. J Manuf Processes 2017;25:185–200.

[21] ISO. Metallic materials — Rotating bar bending fatigue testing. ISO 2010.

[22] ASTM International, "Standard Practice for Conducting Force Controlled Constant Amplitude Axial Fatigue Tests of Metallic Materials," ASTM International, 2015.

[23] Murakami Y. Metal Fatigue- Effects of Small Defects and Nonmetallic Inclusions. Academic Press; 2002.

[24] Pegues J, Roach M, Williamson RS, Shamsaei N. Surface roughness effects on the fatigue strength of additively manufactured Ti-6Al-4V. Int J Fatigue 2018;116: 543–52.

[25] Kahlin M, Ansel H, Moverare JJ. Fatigue behaviour of notched additive manufactured Ti6Al4V with as-built surfaces. Int J Fatigue 2017;101:51–60.

[26] Gockel J, Sheridan L, Koerper B, Whip B. The influence of additive manufacturing processing parameters on surface roughness and fatigue life. Int J Fatigue 2019; 124:380–8.

[27] Balachandramurthi AR, Moverare J, Dixit N, Pederson R. Influence of defects and as-built surface roughness on fatigue properties of additively manufactured Alloy 718. Mater Sci Eng, A 2018;735:463–74.

[28] Shamsaei N, Fatemi A. Small fatigue crack growth under multiaxial stresses. Int J Fatigue 2014;58:126–35.

[29] Nasab MH, Romano S, Gastaldi D, Beretta S, Vedani M. Combined effect of surface anomalies and volumetric defects on fatigue assessment of AlSi7Mg fabricated via laser powder bed fusion. Addit Manuf 2020;34:100918.

[30] Shrestha R, Shamsaei N, Seifi M, Phan N. An investigation into specimen property to part performance relationships for laser beam powder bed fusion additive manufacturing. Addit Manuf 2019;29:100807.

[31] Strano G, Hao L, Everson RM, Evans KE. Surface roughness analysis, modelling and prediction in selective laser melting. J Mater Process Technol 2013;213:589–97.

[32] Nezhadfar PD, Shrestha R, Phan N, Shamsaei N. Fatigue behavior of additively manufactured 17–4 PH stainless steel: Synergistic effects of surface roughness and heat treatment. Int J Fatigue 2019;124:188–204.

[33] Fatemi A, Molaei R, Simsiriwong J, Sanaei N, Pegues J, Torries B, et al. Fatigue behavior of additive manufactured materials: An overview of some recent experimental studies on Ti-6Al-4V considering various processing and loading direction effects. Fatigue Fract Eng Mater Struct 2019;42:991–1009.

[34] Pegues JW, Shao S, Shamsaei N, Sanaei N, Fatemi A, Warner DH, et al. Fatigue of additive manufactured Ti-6Al-4V, Part I: The effects of powder feedstock, manufacturing, and post-process conditions on the resulting microstructure and defects. Int J Fatigue 2020;132.

[35] Romano S, Brückner-Foit A, Brandão A, Gumpinger J, Ghidini T, Beretta S. Fatigue properties of AlSi10Mg obtained by additive manufacturing: Defect-based modelling and prediction of fatigue strength. Eng Fract Mech 2018;187:165–89.

[36] Greitemeier D, Palm F, Syassen F, Melz T. Fatigue performance of additive manufactured TiAl6V4 using electron and laser beam melting. Int J Fatigue 2017; 94:211–7.

[37] NASA. MSFC-SPEC-3717 - Specification for Control and Qualification of Laser Powder Bed Fusion Metallurgical Processes 2017:58. doi:MSFC-SPEC-3717.

[38] Qiu C, Panwisawas C, Ward M, Basoalto HC, Brooks JW, Attallah MM. On the role of melt flow into the surface structure and porosity development during selective laser melting. Acta Mater 2015;96:72–9.

[39] Cunningham R, Narra SP, Montgomery C, Beuth J, Rollett AD. Synchrotron-based x-ray microtomography characterization of the effect of processing variables on porosity formation in laser power-bed additive manufacturing of Ti-6Al-4V. JOM 2017;69:479–84.

[40] Nezhadfar PD, Shamsaei N, Phan N. Enhancing ductility and fatigue strength of additively manufactured metallic materials by preheating the build platform. Fatigue Fract Eng Mater Struct 2020. https://doi.org/10.1111/ffe.13372.